



<https://doi.org/10.1038/s42003-025-07743-3>

Activation of the bacterial defense-associated sirtuin system



Kaixiang Zhu^{1,2,3,10}, Kun Shang^{4,5,10}, Linyue Wang^{1,2,3,10}, Xia Yu^{6,10}, Lei Hua⁴, Weihe Zhang⁶, Bo Qin^{1,2,3}, Jia Wang⁷, Xiaopan Gao^{1,2,3} , Hongtao Zhu^{1,2,3}  & Sheng Cui^{1,2,3} 

The NADase activity of the defense-associated sirtuins (DSRs) is activated by the phage tail tube protein (TTP). Herein, we report cryo-EM structures of a free-state *Bacillus subtilis* DSR2 tetramer and a fragment of the tetramer, a phage SPR tail tube, and two DSR2-TTP complexes. DSR2 contains an N-terminal SIR2 domain, a middle domain (MID) and a C-terminal domain (CTD). The DSR2 CTD harbors the α -solenoid tandem-repeats like the HEAT-repeat proteins. DSR2 assembles into a tetramer with four SIR2 clustered at the center, and two intertwined MID-CTD chains flank the SIR2 core. SPR TTPs self-assemble into a tube-like complex. Upon DSR2 binding, the D1 domain of SPR TTP is captured between the HEAT-repeats domains of DSR2, which conflicts with TTPs self-assembly. Binding of TTPs induces conformational changes in DSR2 tetramer, resulting in increase of the NAD⁺ pocket volume in SIR2, thus activates the NADase activity and leads to cellular NAD⁺ depletion.

Numerous defense systems were found to protect prokaryotic cells from phage infection and inhibit phage propagation. Most of these prokaryotic innate immune systems have been identified and characterized in the past few years^{1–5}; these systems mediate defense against phages through a variety of molecular mechanisms, including nucleotide depletion^{6–12}, small-molecule signaling^{13–15}, membrane disruption^{16–18}, production of anti-phage compounds^{19,20} and reverse transcription of non-coding RNAs^{21,22}.

Defense systems containing SIR2 domains were recently identified to mediate antiviral immunity in prokaryotes. These SIR2-containing defense systems include prokaryotic argonautes (pAgo)²³, the SIR2-HerA³, Thoreris^{2,24}, and defense-associated sirtuins (DSR1 and DSR2)²⁵. A shared common feature of these defense systems is that they all contain the SIR2 domains. The SIR2-domain proteins are present in all kingdoms from prokaryotes to eukaryotes, in which they either catalyze protein deacetylation or ADP-ribosylation employing NAD⁺ as a co-factor^{26,27}. In either case, the SIR2 domain in defense systems exhibits NADase activity; thus it is responsible for depleting NAD⁺ in cells and ultimately lead to cell death after

phage infection. The molecular patterns associated with phage infection that activate these defense systems become an active research field. Nevertheless, the molecular mechanism underlying SIR2 activation remains elusive.

In pAgo systems, the guide RNA-mediated target DNA binding activates the SIR2 subunit^{23,28}, providing an example that nucleic acids may act as molecular patterns for activating the defense systems. In the Thoreris system, cyclic ADP ribose isomers serve as signaling molecules that activate SIR2-encoding effector^{24,29,30}, providing an example of how small compounds may act as secondary messenger for defense systems activation.

Recent studies show that a small protein encoded by a *Bacillus subtilis* phage SPR can activate the bacterial DSR2 system²⁵, offering a paradigm for protein-based activation of defense system. Therefore, DSR2 acts as pattern recognition receptor that detects molecular signatures indicative of pathogen infection, similar to bacterial NLR-like proteins^{31,32}. As a minimal defense system, DSR2 comprises a single polypeptide chain of more than 1000 amino acids, containing an N-terminal SIR2 domain followed by additional domains with unknown structure and function. DSR2 recognizes

¹NHC Key Laboratory of Systems Biology of Pathogens, National Institute of Pathogen Biology, Chinese Academy of Medical Sciences & Peking Union Medical College, Beijing, China. ²Key Laboratory of Pathogen Infection Prevention and Control (Ministry of Education), National Institute of Pathogen Biology, Chinese Academy of Medical Sciences & Peking Union Medical College, Beijing, China. ³State Key Laboratory of Respiratory Health and Multimorbidity, National Institute of Pathogen Biology, Chinese Academy of Medical Sciences & Peking Union Medical College, Beijing, China. ⁴Yanan medical college of Yanan university, Yanan, China. ⁵Beijing National Laboratory for Condensed Matter Physics, Institute of Physics, Chinese Academy of Sciences, Beijing, China. ⁶National Clinical Laboratory on Tuberculosis, Beijing Key Laboratory for Drug-resistant Tuberculosis Research Beijing Chest Hospital, Capital Medical University, Beijing Tuberculosis and Thoracic Tumor Institute, Beijing, China. ⁷Beijing Advanced Innovation Center for Structural Biology, Tsinghua-Peking Joint Center for Life Sciences, School of Life Sciences, Tsinghua University, Beijing, China. ⁸University of Chinese Academy of Sciences, Beijing, China. ⁹Songshan Lake Materials Laboratory, Dongguan, China. ¹⁰These authors contributed equally: Kaixiang Zhu, Kun Shang, Linyue Wang, Xia Yu. ✉ e-mail: gaoxiaopan@pumc.edu.cn; hongtao.zhu@iphy.ac.cn; cui.sheng@ipb.pumc.edu.cn

the tail tube protein (TTP) of phage SPR and subsequently activates the NADase activity of DSR2, leading to bacteria growth arrest²⁵. Nevertheless, it remained unknown how the phage tail tube protein is recognized and how the NADase activity of DSR2 is activated.

In this study, we determined a series of cryo-EM structures to shed light on the activation mechanism for the *Bacillus subtilis* DSR2 system. Our structures reveal that free-state DSR2 forms a long tetramer comprising four N-terminal SIR2 domains clustered at the center, and two pairs of C-terminal domains (CTDs) flanking the SIR2 core on opposite sides. We also provide details for phage SPR tail tube assembly and binding mode between SPR TTPs and DSR2. We show that binding to TTPs rigidifies the folding structure of the DSR2 tetramer, which in turn expands and stabilizes the NAD⁺ pocket in each SIR2 domain, thereby promoting NADase activity. By measuring the levels of cellular NAD⁺, we confirmed that SPR TTPs stimulate the NADase activity of DSR2 in bacteria. Combining our results, we provide a working model for DSR2 system activation.

Results and discussion

Structures of *Bacillus subtilis* DSR2

To investigate the structural basis underlying activation of the DSR2 system in prokaryotes, we first purified and determined the cryo-EM structure of *Bacillus subtilis* free-state DSR2 protein (4.53 Å) (Figs. S1,

S5 and S8; Table S1). Unliganded DSR2 assembles into an elongated tetramer with a dimension of 267 × 117 × 88 Å (Fig. 1a). The DSR2 monomer comprises an N-terminal SIR2 domain, followed by a middle domain (MID) and a C-terminal domain (CTD). Two DSR2 monomers assemble as a *cis*-oriented dimer shaped like an “X”. The two SIR2 domains are joined side-by-side on one end of the dimer, whereas the two CTDs are intertwined such that they switch sides at the other end. To assemble into a tetramer, two DSR2 dimers associate “head-to-head” through their SIR2:SIR2 domains so that four SIR2 domains are clustered at the center, and the CTD dimers are connected to the SIR2 tetramer through the MID domains (Fig. 1a, b). The assembly of four SIR2 domains shows D2 symmetry (Fig. 1a, f). It is worth noting that the link between SIR2 and MID-CTD is flexible because the long axis along the tetramer is not perfectly straight (Fig. 1a, lower panels).

We identified two populations during particle analysis: one containing an intact DSR2 tetramer, and another containing a fragment of the tetramer (Fig. S6). The fragment has lost one CTD pair on one side; the breakage point occurs between the SIR2 and CTD domains. We named this fragment the “free-state DSR2 tetramer fragment” (Figs. 1c, S6 and S9; Table S1). Breakdown of the DSR2 tetramer is unlikely to be caused by protease contamination because SDS-PAGE analysis of the final protein samples did not reveal any degradation products (Fig. S1).

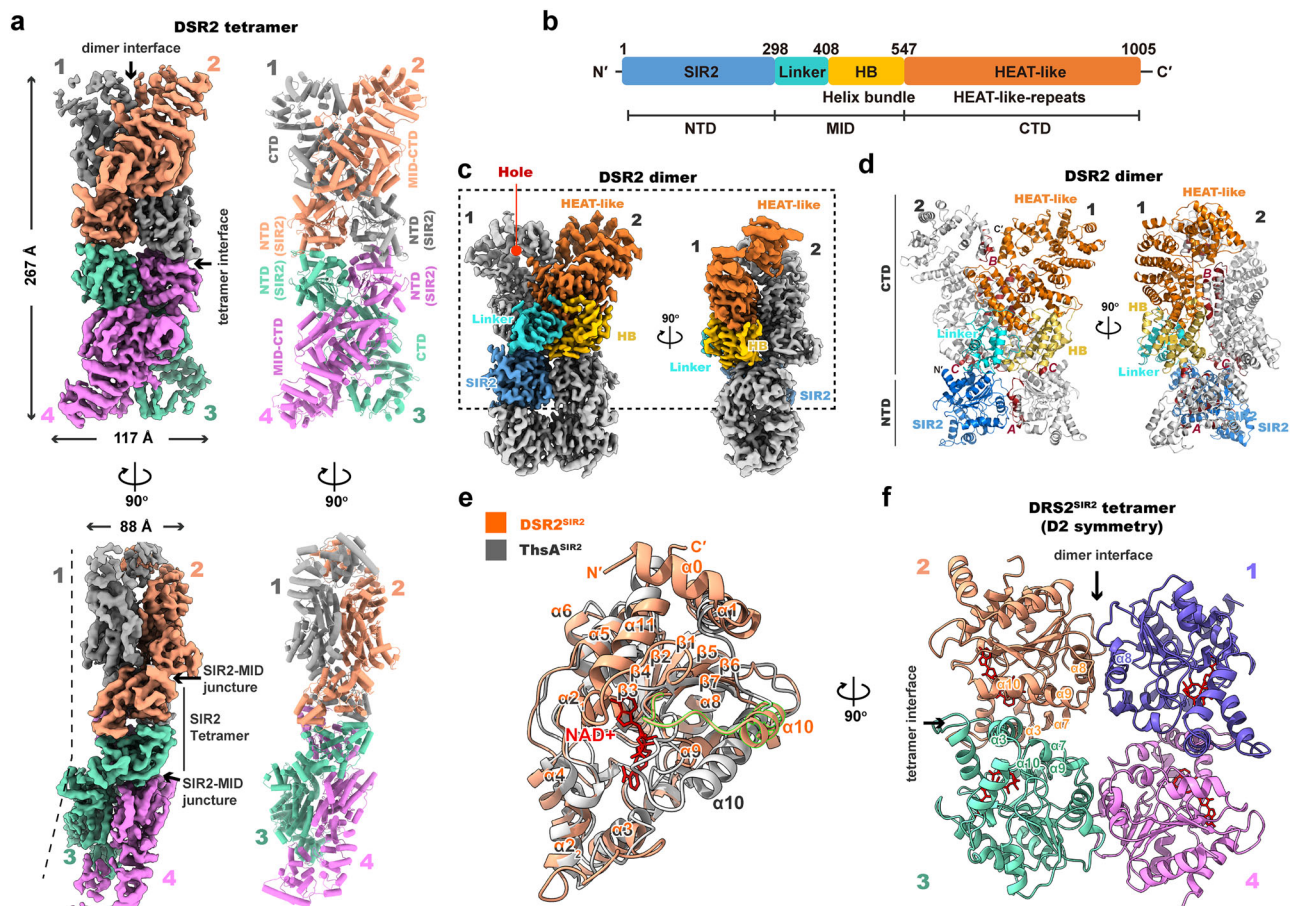


Fig. 1 | Cryo-EM structures of DSR2 tetramer. a Cryo-EM reconstruction of DSR2 tetramer. Cryo-EM densities of the protomers are shown in gray, orange, green and magenta. Upper left; front view of DSR2 tetramer EM densities; lower left; side view the EM densities. Upper right and lower right: atomic model of DSR2 tetramer shown with cylinder helices. **b** Domain organization of DSR2. SIR2, blue; Linker, cyan; helical bundle (HB), gold; HEAT-repeats (HEAT-like), orange. The domain boundaries are indicated. **c** Reconstruction of an incomplete DSR2 tetramer, in which the DSR2-CTD of two protomers are missing. This structure exhibits higher resolution for DSR2 dimer. The front DSR2 protomer is colored by

domains with same color scheme as in (b). Left, front view; right, side view. **d** Ribbon model of the incomplete DSR2 tetramer. Left, front view; right, side view. **e** Structure superimposition of DSR2^{SIR2} (organ) with ThsA^{SIR2} (PDB: 7UXT, gray) with labeled secondary structures. The Helix α_{10} downstream loop, representing the major difference from ThsA, is highlighted by green edges. NAD⁺ (red stick model) was modeled in the putative active site of DSR2^{SIR2} by superimposing it with a SIR2 homolog-NAD⁺ complex (PDB: 1IC1). **f** Assembly of DSR2^{SIR2} within DSR2 tetramer, exhibiting D2 symmetry. Helices at the SIR2:SIR2 interfaces are labeled.

A 3D reconstruction of the DSR2 fragment yielded better EM densities, with higher resolution (3.74 Å) (Figs. S6 and S9; Table S1). We therefore used this reconstruction to facilitate model building (Fig. 1c, d). A search for structural homologs using the Dali server³³, we found DSR^{SIR2} (residues 1–298) shares highest structural similarity with *Streptococcus equi* ThsA^{SIR2} domains (SeThsA^{SIR2}, PDB: 7UXT), which gave a Dali Z-score of 23.9 and a rmsd of 2.5 Å for 250 aligned Ca atoms. By contrast, rather poor structural similarity was identified for the MID-CTD region of DSR2 (residues 299–1005). Depending on the folding pattern, we further divided the MID domain (299–547aa) into two subdomains: Linker, helical bundle (HB). No structural homologs were found for the Linker or HB domains. We denoted the CTD (548–1005aa) of DSR2 as “HEAT-like repeats” (HEAT-like, Fig. 1b, c), because the Dali search identified that the CTD is distantly related to the B subunit of PP2A in the Sgo1-AB’C PP2A complex (PDB: 3FGA) harboring eight HEAT (Huntington, Elongation Factor 3, PR65/A, TOR)-repeats, Z-score = 7.9 (Fig. S2d, e).

The Linker (residues 299–408) is a mixed α/β domain bridging the SIR2 and CTD. The loop connecting the SIR2-Linker is extended and unstructured (residues 290–305), which might explain the flexibility of the long tetramer at this junction (Figs. 1a, c, S2). The HB (residues 409–547) is a twisted helical bundle comprising several antiparallel α -helices. The HB lies side-by-side with the Linker domain and sits on top of the DSR2^{SIR2} of the neighboring DSR2 protomer (Figs. 1c, d, S2). The HEAT-like domain (residues 548–1005) is buttressed by both Linker and HB domains, from where it extends outward to form the apices of the DSR2 tetramer. We calculated the interfacial area of DSR2 dimer interface using PISA: the areas between DSR2 1-2 and 3-4 are 3503.2 Å² and 3479 Å², respectively, which involve interactions between the SIR2:SIR2, HB:SIR2, and HEAT-like:HEAT-like domains (Fig. 1a, d). The dimer:dimer interfacial areas between DSR2^{SIR2} 2-3 and 1-4 are 971.2 Å² and 897.6 Å², respectively (Fig. 1f).

The DSR2 HEAT-like domain contains 11 tandem α -helices pairs of various lengths, with ~30–50 residues per helix-turn-helix unit (Figs. 1d, S2). Because it lacks sequence similarity with typical HEAT proteins, we denoted it as the HEAT-like domain. Similar to the architecture of canonical HEAT proteins, the HEAT-like repeats of DSR2 stack in parallel with right-handed twists, and fold into a larger C-shaped module with a narrow opening. In the dimer, the openings of the two C-shaped modules are joined (Figs. 1d, S2). These hollow structural features suggest loosely folded regions at two ends of the long tetramer, which coincides with the poor EM densities in that region.

DSR2^{SIR2} domain exhibits a canonical Rossmann-fold. It contains a seven-stranded parallel β -plane (β 3– β 4– β 2– β 1– β 5– β 6– β 7) surrounded by multiple α -helices, with connecting loops on both sides (Figs. 1e, S3). Helices α 1, α 5, α 6, and α 11 pack against the β -plane on one side, and helices α 7– α 10 pack against the β -plane on the opposite side. Additionally, an insertion (α 2– α 4) extends between β 1 and α 5, and helices α 2– α 3– α 4 constitute a triangular protrusion (Figs. 1e, S3).

We modeled a NAD⁺ molecule in DSR2^{SIR2} structure by superimposing it on a SIR2 homolog-NAD complex from *Archaeoglobus fulgidus* (PDB: 1ICI) and identified a putative NAD⁺ binding pocket harboring conserved catalytic residues S51, N133, D135, and H171 (Figs. 1e, S3). By comparing the structures of DSR2^{SIR2} and ThsA^{SIR2}, we found that the NAD⁺ pocket of DSR2^{SIR2} is more open than that of ThsA^{SIR2}; this is because the α 10 helix of DSR2^{SIR2} at the pocket entrance is evidently shorter than that of ThsA^{SIR2} (Fig. 1e).

Structure of *Bacillus* phage SPR tail tube protein

To investigate the role of *Bacillus* phage SPR TTP in DSR2 activation, we determined TTP structure alone (Figs. 2, S7, S9; Table S2) and in complex with the DSR2 tetramer (Figs. 3, S8, S9; Tables S1, S2). The SPR TTP monomer is a 264 aa polypeptide annotated as a hypothetical protein (GenBank: UNY48585.1). We found that recombinant SPR TTP eluted from a size-exclusion column is a high-ordered species (Fig. S1d), indicating self-oligomerization. Our cryo-EM micrograph of this high-ordered species revealed segments similar to the non-contractile tail tubes of *Siphophages*.

The segments were of varying length, and some were straight whereas others were bent (Fig. 2a).

A 3D reconstruction of the SPR TTP segments yielded a right-handed helical tube structure (3.43 Å) comprising stacks of hexameric rings (Figs. S7, S9). Each ring comprises six TTP units, and the hexameric rings are piled up with a pitch of 44.0 Å and a twist of 18.3° (Fig. 2b). We observed clear EM densities for the main tube body and the decorations protruding from the tube body, which gave an overall outer and inner diameter of 132.7 Å and 37.7 Å, respectively (Fig. 2b, c). We modeled an ideal double-stranded DNA into the central tunnel of the tube, demonstrating that the tunnel is sufficient to allow double-stranded DNA to pass through (Fig. 2d).

A SPR TTP monomer is a two-domain unit comprising domain 1 (D1) forming the main tube body and domain 2 (D2) forming the decorations (Figs. 2f, S4); a short C-terminal region (residues 242–264) was disordered in the structures. The D1 domain contains a two-layer antiparallel β -planes sandwich flanked by a short helix α 1 (Figs. 2f, S4). To assemble a hexameric ring, the inner β -planes (β 2– β 5– β 15– β 16) of six TTP units form a continuous β -barrel that delineates the inner surface of the tube (Fig. 2g). The tube interior is negatively charged, implying that it repels DNA strands so that the viral genome can slide through. Six outer β -planes (β 1– β 13– β 14– β 17) and the flanking helices form the outer layer of the tube. Helix α 1 is oriented parallel to the tube axis and is wedged between neighboring β -planes (Fig. 2g). The D2 domain forms the decoration layer coating the tube body, in which the stem portion of D2 is situated above the tube body and the Ig-like portion of D2 protrudes from the tube body (Fig. 2h).

A search using the Dali server identified several bacteriophage tail tube structures that are similar to our SPR TTP tube; of these the YSD1 phage major tail tube (PDB: 6XGR) was the top hit, with a Dali Z-score 13.9 and a rmsd 4.4 Å. The SPR TTP D1 domain is also similar to the Hcp protein from the *C. jejuni* type VI secretion system (PDB: 6A2V; Z-score 10.4, rmsd 3.3 Å).

Intermolecular interactions among the TTP units within the SPR tail tube involve contacts between TTP units within the hexameric ring and contacts between the ring stacks. The intra-ring TTP-TTP contacts include two interunit β -sheet interactions flanking the D1 domain. One interaction involving the antiparallel β -sheet is between β 2 of one TTP unit and β 15 of the adjacent unit, joining six inner β -planes into a β -barrel (Fig. 2g, h). Another antiparallel β -sheet interaction occurs between β 12 of one TTP unit and β 17 of the adjacent unit, thereby joining helix α 1 with the outer β -plane to form the outer layer of the tube (Fig. 2g, h). Inter-ring contacts involve primarily four β -hairpins (β -h) protruding from the β -plane sandwich of D1; namely, β -h1 (β 3-to- β 4), β -h2 (β 13-to- β 14), β -h3 (β 15-to- β 16) and β -h4 (β 15-to- β 16) (Fig. 2f, h). Whereas β -h1 and β -h4 extend into the hexameric ring below, β -h2 and β -h3 extend into the ring above (Fig. 2h). Hairpin β -h1 is considerably longer than the other hairpins, and it extends deeply into the D1 domains of the hexameric ring below, suggesting that β -h1 plays a pivotal role in ring-ring assembly.

Structures of the DSR2-SPR TTP complex

When we tried to assemble the DSR2-SPR TTP complex, neither mixing separately purified DSR2 and SPR TTP nor co-expressing the two components resulted in a stable complex. Therefore, we co-expressed a catalytic mutant (DSR2 H171A) with SPR TTP (Fig. S1) and obtained a qualified sample for cryo-EM studies. We then determined the cryo-EM structure of tetrameric DSR2-SPR TTP complex to 4.66 Å and SPR TTP bound DSR2 tetramer incubated with NAD⁺ to 4.40 Å (Figs. S7–S9). Similar to the situation of free-state DSR2 tetramer, we identified two other particle populations from samples incubated with or without NAD⁺ containing a DSR2 tetramer fragment lacking two CTDs on one side; however, this fragment was still bound by two SPR TTPs. We designated these as the SPR TTP bound DSR2 tetramer fragment and SPR TTP bound DSR2 tetramer fragment with NAD⁺. Reconstruction of these populations yielded higher-resolution structure (4.03 Å/4.27 Å) and allowed accurate model building (Figs. S7–S9). However, neither the structure of the tetrameric DSR2-SPR

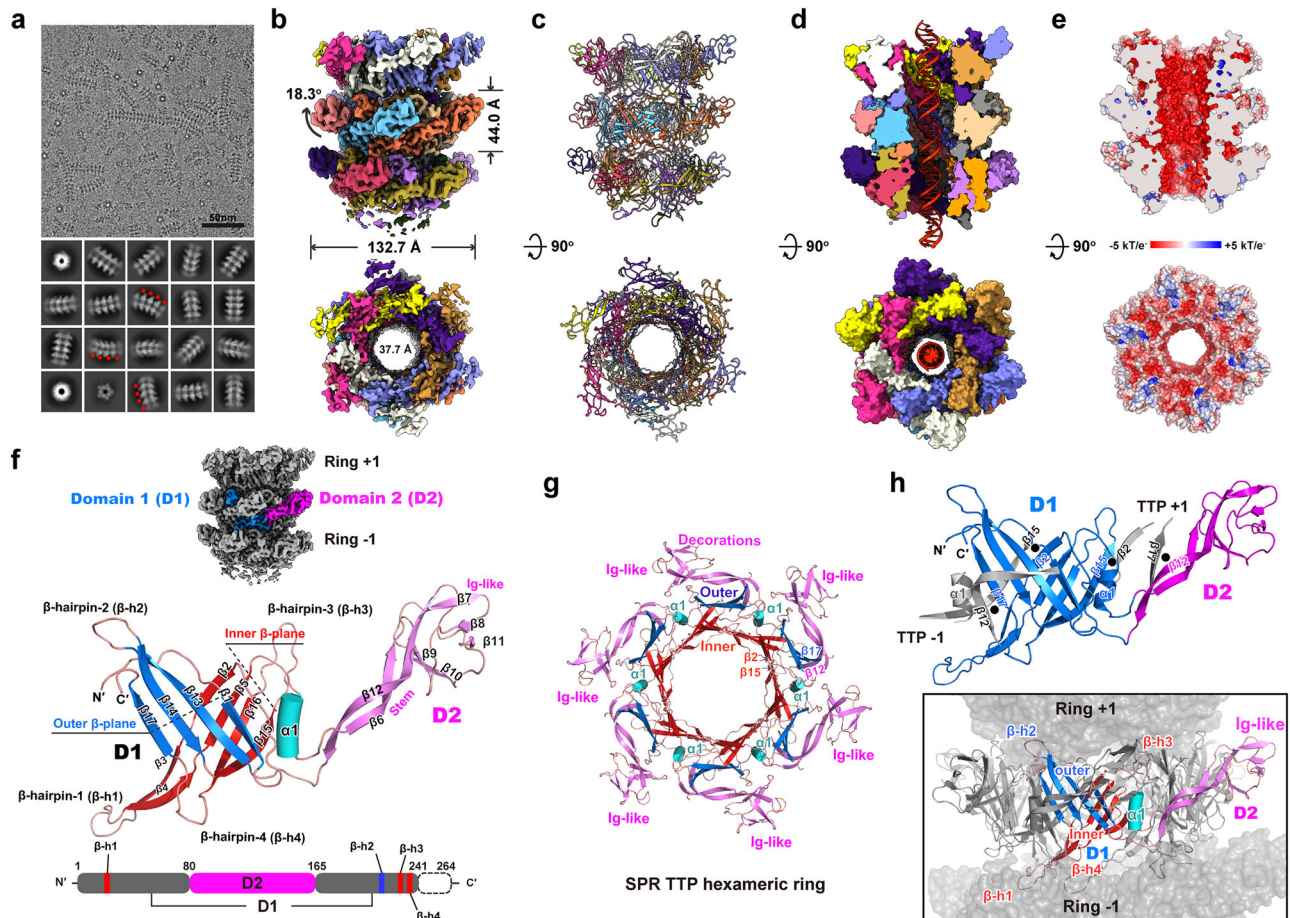


Fig. 2 | Cryo-EM structures of SPR phage tail tube. **a** Upper, representative cryo-EM micrograph of SPR tail tube formed by self-assembled SPR tail tube proteins (TTP); scale bar = 50 nm. Lower, various 2D class averages of SPR tail tube. Red dots indicate the curvature of SPR tail tube. **b** Cryo-EM reconstructions of SPR tail tube colored by chains; six TTP chains form a hexameric ring and three layers of TTP rings are shown. Top: side view, bottom: top view. **c** Ribbon model of SPR tail tube; top: side view, bottom: top view. **d** Cut-away view of SPR tail tube with an ideal B-form DNA double helix (red ribbon) modeled in the central tunnel. Top: side view, bottom: top view. **e** Cut-away view of SPR tail tube. The surface electrostatic potential is plotted as a red-to-blue gradient from electronegative to electropositive. **f** Upper, domain organization of SPR tail tube protein (TTP), the outer β -plane of D1 is colored blue, the inner β -plane of D1 is colored red, the α 1 helix of D1 is colored

cyan; D2 is colored magenta. Lower, ribbon model of SPR TTP with labeled secondary structures. Four important β -hairpins of D1 domain (β -h1, β -h2, β -h3 and β -h4) are indicated. **g** Top view of a TTP hexameric ring colored by inner β -barrel (inner tube layer, red), outer β -planes (blue) and α 1 helix (cyan) wedged between them. The six D2 domains (magenta) form decorations that protrude from the tube body. **h** Top, SPR TTP ribbon model colored by domains, D1 blue, D2 magenta. Key TTP-TTP interactions within the hexameric ring are indicated with black dots. β -sheets involved in the interactions are labeled. Bottom, side view of a SPR tail tube with the central TTP hexameric ring shown in ribbon model; the ring stacked above (Ring +1) and below are shown with semitransparent molecular surface (gray). Four hairpins (β -h1-4) extending from the D1 domain mediate ring-ring interactions.

TTP complex after incubation with NAD^+ nor the structure of the tetramer fragment of DSR2-SPR TTP showed a clear density for NAD^+ .

The binding of SPR TTP altered the overall dimensions of DSR2 tetramer; particularly, the height was reduced from 267 Å to 255 Å, whereas the width was increased from 88 Å to 94 Å (Fig. 3a). Four SPR TTP monomers occupied four funnel-shaped binding cavities formed between the intertwined DSR2 CTDs (Fig. 3a), rendering large interfacial areas of 3814 to 4051 Å² for each cavity (average 3930 Å²). The binding mode of the SPR TTP resembles a “pushpin” penetrating paper. Whereas the β -plane sandwich of SPR TTP (like a pushpin handle: -SPR-TTP-1) was fully accommodated in the cavity on one side of the tetramer, the apex of hairpin β -h1 (like a pin tip: -SPR-TTP-2) penetrated through to the other side (Fig. 3b).

Comparing the TTP structures within the assembled tail tube revealed that the TTP bound by DSR2 underwent evident conformational changes (Fig. 3c). Whereas the entire D1 domain was captured by the main DSR2 cavity, the D2 domain was disordered, suggesting that this portion may not be recognized by DSR2. The β -plane sandwich of D1 presents a rigid core because its fold remains largely unchanged upon binding to DSR2. By

contrast, the four β -hairpins, the α 1 helix and the connecting loops around the β -sandwich core shifted from their original positions (Fig. 3c).

A detailed DSR2-SPR TTP interaction is illustrated in Fig. 3d, showing nearly all parts of the D1 domain are buried in the main DSR2 cavity (Fig. 3d). The main cavity is formed by the HB and HEAT-like domains of one DSR2 molecule, and by the Linker and HEAT-like domains of the other DSR2. The front entrance of the cavity has an overall triangular shape, complementary to the shape of the TTP D1 domain. On the rear side of the cavity, a small hole is formed by the HEAT-like domain, and the β -h1 hairpin of D1 extended into the hole (Fig. 3b, d). It is worth noting that no direct contacts were found between the bound TTPs to the DSR2 domains. Hairpin β -h3 of D1 is oriented proximate the DSR2 domains; the shortest distance was 19.4 Å (Fig. 3d left).

The TTP-TTP interactions found within SPR tail tube conflict with DSR2-TTP interactions found in the DSR2-TTP complex (Fig. 3e). In the presence of DSR2, the α 44-to- α 45 loop of DSR2 replaces TTP (-1) β 12 to pair with TTP β 17 (Fig. 3d right ① & e). The α 26-to- α 27 loop of DSR2 replaces TTP (-1) β 15 to pair with TTP β 2 (Fig. 3d right ② & e). Two α 1 helix flanking the outer β -plane in the context of TTP hexameric ring are replaced

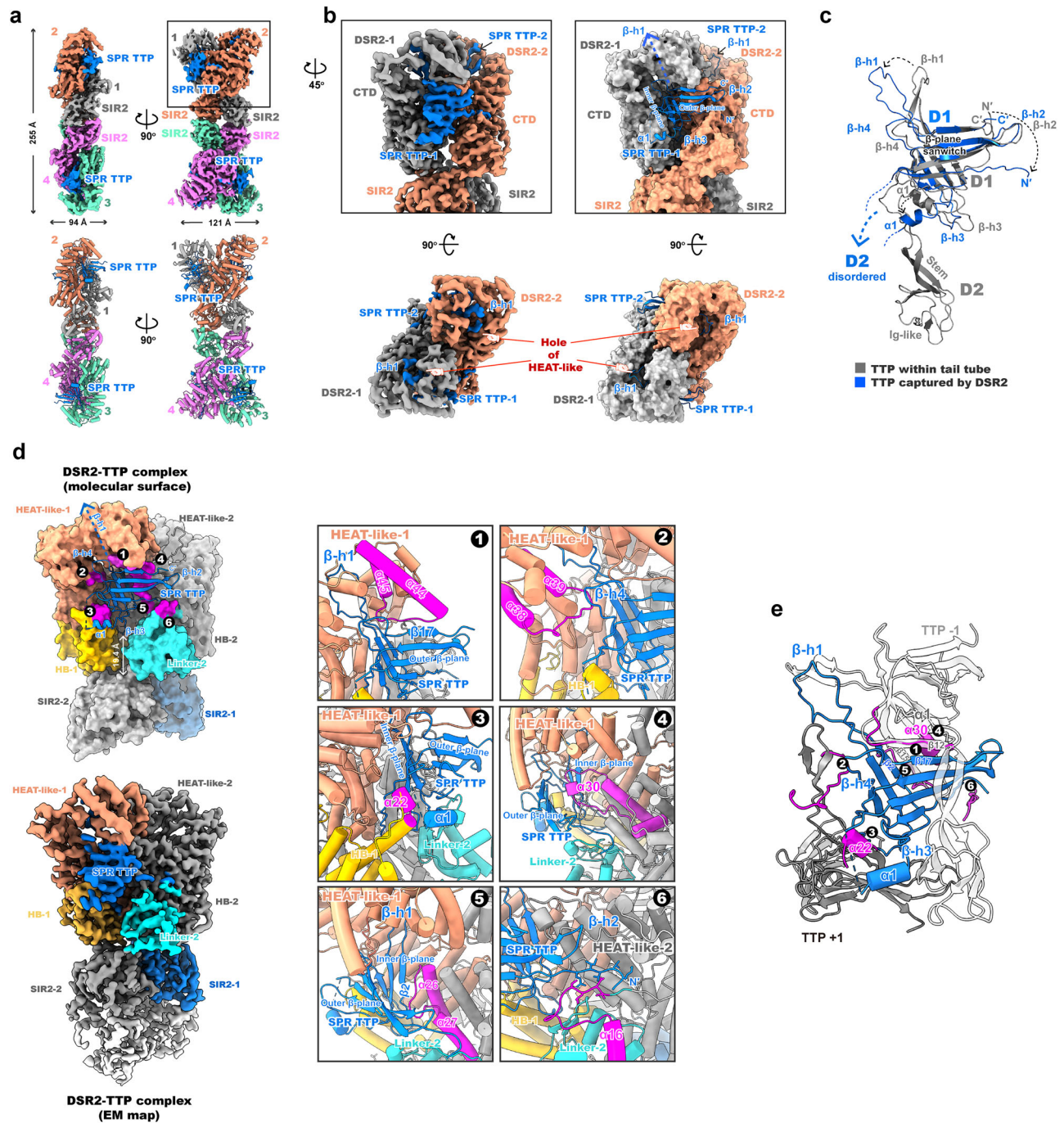


Fig. 3 | Cryo-EM structures of DSR2 bound to the SPR TTP. **a** Cryo-EM reconstruction of DSR2 tetramer (same color scheme as in Fig. 1a) complexed with four SPR TTPs (blue). Upper left, front view of EM densities of DSR2-SPR TTP complex; lower left, side view the EM densities. Upper right and lower right, atomic model of DSR2-SPR TTP complex shown as cylinder helices. **b** Magnified view of the SPR TTP binding site formed between two DSR2 CTDs (colored gray and orange). Upper left, side view of cryo-EM densities, lower left, top view of cryo-EM densities. Upper right and lower right, side and top view of atomic model of DSR2-SPR TTP complex, in which DSR2 protomers are shown as a molecular surface model, and TTP is shown as a ribbon model. Three β -hairpins of SPR TTP (β -h1, β -h2 and β -h3) that are important for DSR2 binding are indicated. **c** Superimposition of the SPR TTP structure within tail tube (gray) onto its structure in complex with DSR2 (blue). **d** Interaction details of the DSR2-TTP

complex. An SPR TTP binding pocket formed between DSR2-1 and DSR2-2 is shown as a molecular surface model; the EM density map of the DSR2-TTP complex is shown below with the same color code. The bound SPR TTP is shown as a ribbon model. Domains constituting TTP binding cavity include the HEAT-like (orange) and HB (gold) from DSR2-1 and the HEAT-like (gray) and Linker (cyan) from DSR2-2. While SPR TTP β -h1 extends into the hole of DSR2-1 HEAT-like, six more contacts with DSR2 (1–6) are indicated and highlighted in magenta. Boxes on the right, magnified views of the DSR2-TTP interactions 1–6. **e** The SPR TTP structure (blue) bound by DSR2 regions (magenta) illustrate in (d) (1–6, magenta) are shown as ribbon models. The neighboring TTP molecules (TTP -1 and TTP +1) in the context of TTP hexameric ring are superimposed here and shown as semitransparent gray ribbon models to highlight conflicting regions between TTP-TTP interaction and DSR2-TTP interaction.

by DSR2 α 22 and α 30 helices, respectively (Fig. 3d right 3, 4 & e). Additional interactions include the α 38-to- α 39 loop of DSR2 with the TTP β -h4 hairpin (Fig. 3d right 2), and an N-terminal loop of TTP (residues 3–8) with the loop downstream of DSR2 α 16 (Fig. 3d right 6).

Phage SPR and phi3T belong to the *B. subtilis* SP- β group phages³⁴. The TTP of SPR shares ~40% amino acid sequence identity with the TTP of phi3T. We aligned the amino acids sequence of their TTPs and mapped the DSR2 binding regions identified from the cryo-EM structures (Fig. 3d) on

the sequences (Fig. S5). Most regions on SPR TTP recognized by DSR2 are conserved, suggesting DSR2 might be able to bind other phage TTPs with similar sequence and structure akin to SPR TTP. Indeed, Garb et al. found that phage SPbeta/phi3T TTPs could bind DSR2, albeit with lower affinity than that for the SPR TTP-DSR2 interactions²⁵. Nevertheless, further experiments are required to validate whether SPbeta/phi3T TTPs could activate the DSR2 system.

The α -solenoid tandem-repeat proteins, such as the HEAT-repeats or the tetratricopeptide-repeats (TPRs), etc., share a common structural feature: the tandem repeats of antiparallel α -helical hairpin³⁵. Such a scaffold allows versatile protein partner binding. The tandem-repeat motifs were also identified in bacterial antiphage systems. For example, the bacterial NLR-related proteins are composed of an N-terminal Effector domain, a central NACHT domain and a C-terminal Sensor domain. In some NLR-related protein families, their Sensor domains contain HEAT or TPR motifs that are implicated in recognizing phage infection stimuli³⁶. Likewise, the Avs protein families also contain a C-terminal TRP-like sensor domains that can bind the cognate phage-encoded proteins to activate the Avs phage-defense system³². Here, we provide yet another example that the HEAT-like repeats play a role in sensing phage TTPs. We show that the HEAT-like domain of DSR2, structurally similar to the HEAT-repeats in the Sgo1-AB'C PP2A complex, could recognize the D1 domain of SPR TTP to activate the DSR2 system.

Collectively, our structural analyses indicate that the DSR2 system recognizes the entire TTP D1 domain through the HEAT-like domain of DSR2 in a structure-specific manner and the DSR2-TTP interaction may prevent self-assembly of SPR TTP.

SPR TTP induces conformational changes and SIR2 activation

To understand SPR TTP-induced conformational changes in DSR2, we superimposed free-state DSR2 tetramer with the TTP bound DSR2 with respect to their central SIR2 domains (Fig. 4a) and compared the two structures side-by-side (Fig. 4b). We observed subtle changes in SIR2 domain organization, whereas the HEAT-like domains underwent remarkable conformational changes (Fig. 4c, d). The most evident domain movement involved the HEAT-like repeats directly interacting with the SPR TTP D1 domain. For example, the $\alpha 44$ -to- $\alpha 45$ module on top of DSR2 tetramer rotated down to catch the target (Fig. 4c, right, d). Collectively, SPR TTP binding induces a conformational transition in the DSR2 tetramer, from a relatively loose state (particularly in HEAT-like domains) to a rigid state.

Nevertheless, the above analyses did not fully clarify a key question: given no direct contacts were identified between the bound TTPs and SIR2 domains (Fig. 3), how is the NADase activity triggered? One possibility is that TTP binding rigidifies the folding of the DSR2 tetramer, which may lead to changes in the NAD⁺ pockets in the SIR2 domains. To test our hypothesis, we compared the volume of the NAD⁺ binding pockets in SIR2 in the absence and presence of SPR TTP using software Caviar³⁷. Caviar identified four NAD⁺ pockets in free-state SIR2 tetramer; each NAD⁺ pocket in an SIR2 domain had an average volume of 440 Å³. Upon SPR TTP binding, the NAD⁺ pockets expanded dramatically, the average volume of each NAD⁺ pocket more than doubled in volume, reaching 1028 Å³ (Fig. 4e). SPR TTP-induced NAD⁺ pocket expansion may benefit substrate accessibility and, in turn, the NADase activity of the SIR2 domain.

To support our structural investigation, we carried out viability assays and measured cellular NAD⁺ activity in the presence of the DSR2-TTP complex. We initially employed two *E. coli* strains, BL21-AI and MG1655, for the viability assays (Fig. 5a). Ectopic expression of DSR2 and SPR TTP was separately inducible by isopropyl β -D-thiogalactopyranoside (IPTG) or L-arabinose (L-Ara), respectively. As shown in Fig. 5a, whereas expression of DSR2 or SPR TTP alone had negligible impact on bacteria viability, co-expression of the two components resulted in remarkable cell growth inhibition. Further, the NADase catalytic mutants harboring H171A and N133A-H171A mutations abolished the DSR2-TTP complex-elicited cell death (Fig. 5a). Because the MG1655 strain was more susceptible to the

DSR2-TTP complex (Fig. 5a), we used MG1655 for the following experiments. Next, we assessed bacteria growth in liquid media by recording optical density (OD) measured at 600 nm (Fig. 5b). Likewise, whereas MG1655 cells expressing the DSR2-TTP complex suffered from significant cell growth inhibition, the other constructs, expressing DSR2, TTP alone or co-expressing TTP with the DSR2 catalytic mutants, had a negligible effect on bacteria growth curves (Fig. 5b).

To understand whether the DSR2-TTP complex-elicited bacteria death was attributed to cellular NAD⁺ depletion, we measured intracellular NAD⁺ levels of *E. coli* expressing DSR2, SPR TTP alone or the DSR2-TTP complexes (Fig. 5c). Consistent with the viability assays, expression of the DSR2-TTP complex significantly reduced intracellular NAD⁺ levels (Fig. 5c left and middle), but co-expression of SPR TTP with the DSR2 catalytic mutant, DSR2-H171A or DSR2-N133A-H171A, were ineffective. To investigate whether stoichiometry of DSR2-TTP could affect cellular NAD⁺ depletion, we fixed the IPTG concentration for DSR2 induction while varying the L-Ara concentration for TTP induction (Fig. 5c right). By lowering the concentration of L-Ara for induction, we observed that the intracellular NAD⁺ concentration gradually increased (Fig. 5c right), suggesting that the NADase activity of DSR2 was downregulated due to a short supply of SPR TTP. When we induced the TTP expression using 0.001% of L-Ara, the cellular NAD⁺ level almost resumed to that of the no inducer control (Fig. 5c right). These results support our structural characterization of the DSR2-TTP complex, which supports that binding of SPR TTP activates the NADase activity of DSR2 SIR2 domain allosterically; as a result, the cellular NAD⁺ is depleted and ultimately leads to cell death.

To validate whether the cryo-EM structures of DSR2-TTP are functionally relevant, we conducted structure-guided mutagenesis studies (Fig. 5d, e). We purified recombinant DSR2 tetramers and SPR TTP monomers separately for an in vitro SPR TTP-activated NADase assay. To solve the problem that SPR TTP self-assembled into high-order oligomers, we followed a protocol described by Zhang et al.³⁸. Briefly, a glutathione S-transferase (GST) tagged SPR TTP was expressed to prevent TTP self-oligomerization. The GST tag was then removed by PreScission protease and the monomeric untagged SPR TTP was acquired by size-exclusion chromatography. Based on the cryo-EM structure of DSR2-TTP complex, we engineered a large selection of mutations in five key regions in the DSR2-TTP complex, namely the DSR2-SIR2 interface, the SIR2-SIR2 interface, the DSR2-TTP interface on TTP side, the DSR2-TTP interface on DSR2 side and the DSR2-DSR2 interface (Fig. 5e). Deletion of SPR TTP 34–38 aa loop resulted in ~50% loss of the NADase activity. By contrast, mutations or deletions of all other regions led to severe loss (>80%) of NADase activity (Fig. 5d). The TTP 34–38 aa loop is located on the β -h1 hairpin of the D1 domain (Fig. 2f). Hairpin β -h1 extended into the hole formed by the DSR2 HEAT-like domains, and the intermolecular contacts were mainly hydrophobic interactions (Fig. 3). It was therefore possible that deletion of this small loop on β -h1 hairpin had moderate impact on TTP binding. Collectively, the mutagenesis results indicate that the assembly of the DSR2 tetramer and binding of SPR TTP by the HEAT-like domains (as illustrated by the cryo-EM structures) are important to the TTP-activated NADase activity of the DSR2 system.

The activation mechanism of SIR2-containing defense systems remains incompletely understood. One proposed mechanism for NADase activation in the prokaryotic Argonaute-associated SPARSA system involves subtle structural movements of the H186-containing loop upon binding of gRNA-tDNA. This creates a cavity in which two water molecules can accumulate and carry out a nucleophilic attack on C1' of NAD⁺, a critical step for activating SIR2 NADase²⁸. In the Theoris antiviral system, recent studies have demonstrated that gcADPR signaling molecules bind to the ThsA SLOG domain, thereby initiating the assembly of ThsA tetramers into helical filaments. This assembly stabilizes the active conformation of the ThsA SIR2 domain, resulting in enhanced NADase activity³⁰. However, the activation mechanism of SIR2 in the SIR2-HerA system during phage infection remains poorly understood^{10,12}. In this study, we propose that DSR2 is activated allosterically through its interaction with SPR TTPs. The

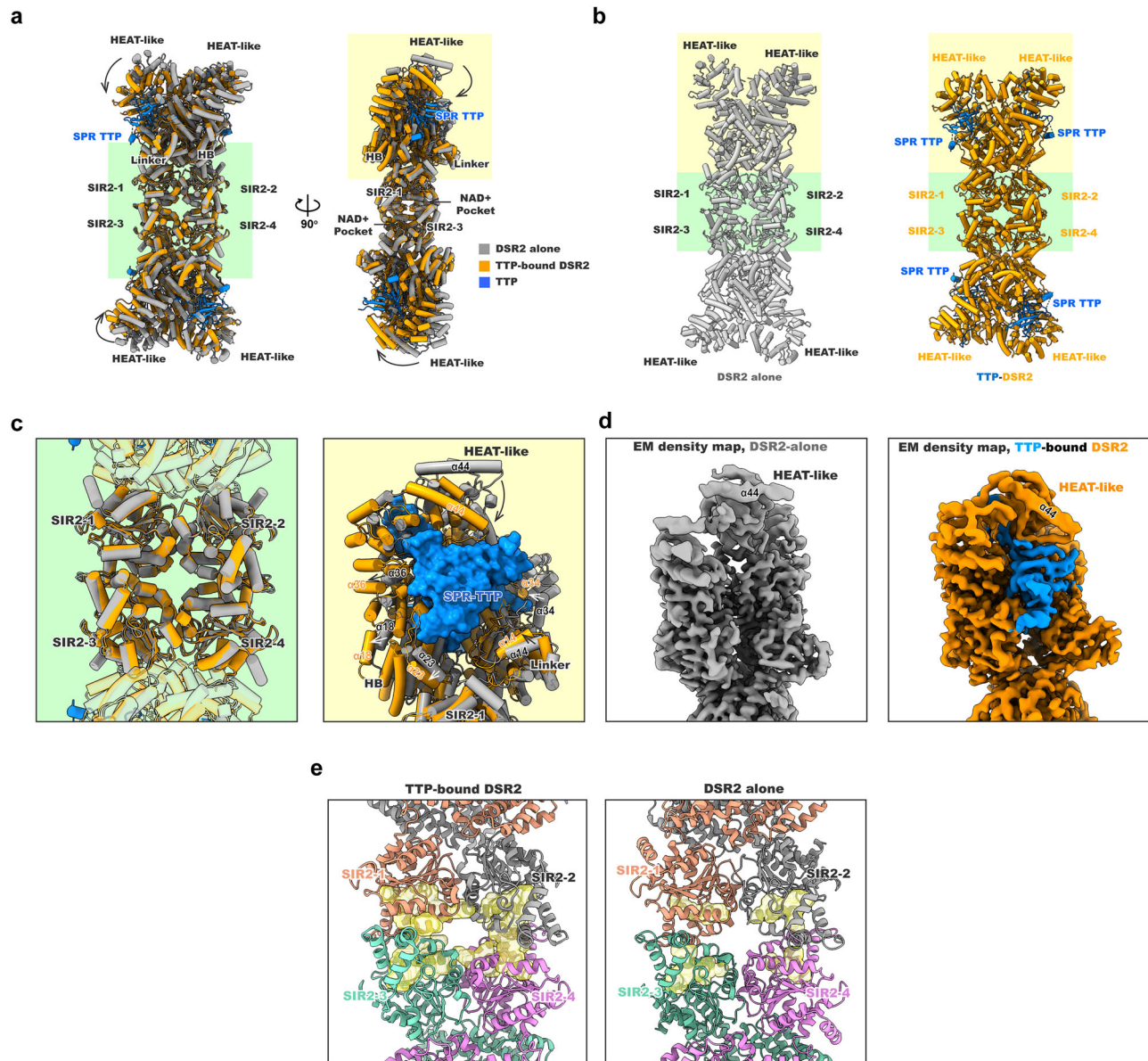


Fig. 4 | Activation of DSR2 by SPR TTP. a Structural comparison between unliganded DSR2 tetramer and SPR TTP (blue) bound DSR2 tetramer (shown as cartoon models). Unliganded DSR2 tetramer is colored gray with semitransparent surface, and SPR TTP bound DSR2 tetramer is colored orange. Evident structural rearrangement at the tip of HEAT-like domains is indicated by arrows and highlighted by yellow background. Structural comparison at SIR2:SIR2 interfaces is highlighted by green background. **b** Cartoon models of unliganded DSR2 tetramer (gray, left) and SPR TTP (blue) bound DSR2 tetramer (orange, right); the models have the same orientation as the structure in (a) (left). **c** Left, structural details at SIR2:SIR2 interfaces; right, details of structural rearrangement at HEAT-like domains. **d** EM density maps of unliganded DSR2 tetramer (gray, left) and SPR TTP (blue) bound DSR2 (orange, right). **e** Cavities at putative SIR2 active site identified by software CAVIAR are shown with semitransparent space. In unliganded DSR2 tetramer, cavity size at the putative SIR2 active site is much smaller than the cavity size identified in the TTP bound DSR2 tetramer.

interaction between DSR2 and SPR TTP prevents the self-assembly of SPR TTPs. Binding of SPR TTP triggers significant conformational alterations in the DSR2 tetramer, enhancing the structural rigidity and expanding the NAD^+ binding pocket within the SIR2 domains. This process stabilizes the active conformation of the $\text{DSR2}^{\text{SIR2}}$ domain, enabling the rapid consumption of NAD^+ . Additionally, the interface of the $\text{DSR2}^{\text{SIR2}}$ domain aligns with tetramerization and helical interfaces of ThsA, suggesting a conserved activation and regulation strategy for the Thoeris and DSR antiviral system.

Conclusion

Combining our structural and mutagenesis studies, we propose a working model for DSR2 activation and its role in defense against phages (Fig. 5f). Assembly of the phage tail tube is a key step during virus replication in

bacteria. During translation of viral proteins, TTP monomers (the building blocks of the tail tubes) are recognized by DSR2 CTDs before they self-assemble into tail tubes (Fig. 5f); specifically, the D1 domain of TTP is recognized and captured in the cavities formed by the DSR2 HEAT-like domains (Fig. 4a–d). Because the DSR2–TTP interaction prevents the self-assembly of TTP into tail tubes, DSR2 might inhibit viral replication by depleting TTP monomers. Upon binding TTPs, DSR2 undergoes profound conformational changes that rigidify its folding structure and ultimately expands the NAD^+ pockets in the $\text{DSR2}^{\text{SIR2}}$ domains. Expansion of the NAD^+ pocket may favor substrate binding, thereby stimulating NADase activity. Finally, the stimulated NADase activity of DSR2 depletes the cellular pool of NAD^+ , causing growth arrest or death of infected bacteria. During our submission, the associated structures of the DSR2 system have also been independently confirmed by other groups^{38–40}.

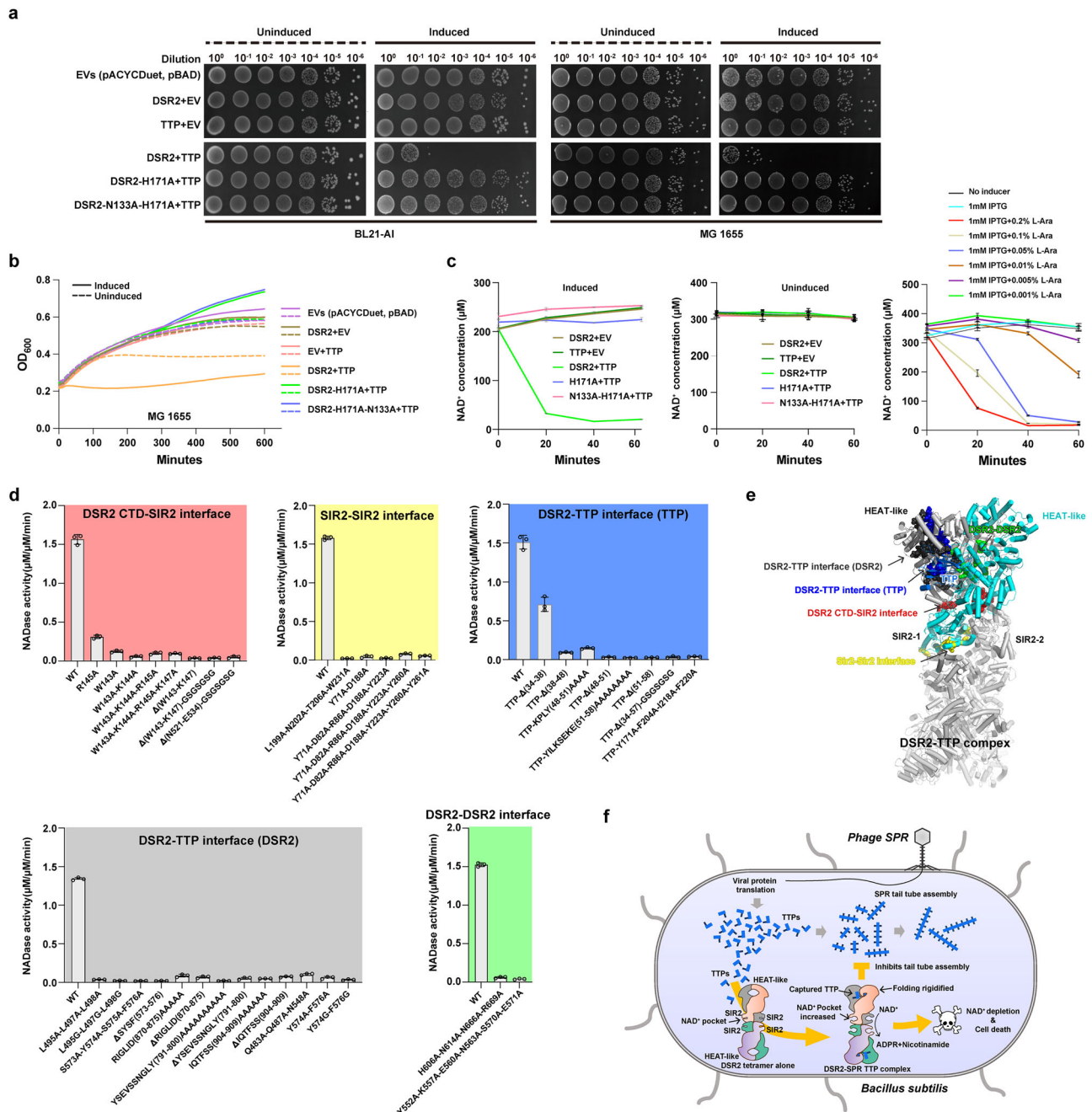


Fig. 5 | Viability assays and mutagenesis studies. a Viability assays of *E. coli* cells (BL21-AI and MG1665 strains) ectopically expressing indicated DSR2 variants (pACYCDuet) and SPR TTP (pBAD). The expression was either induced (1 mM IPTG and 0.2% L-Ara) or uninduced. **b** Growth curves of *E. coli* MG1655 expressing indicated DSR2 variants and SPR TTP. The expression was induced by adding 1 mM IPTG and 0.2% L-Ara when the bacteria were grown to OD₆₀₀ between 0.2 and 0.3. Each curve represents the mean \pm SD of $n = 3$ independent biological replicates. **c** Intracellular NAD⁺ concentration of bacteria expressing indicated DSR2 variants and SPR TTP. Left, the expressions were induced; middle, the expressions were uninduced. Right, NAD⁺ level of bacteria co-expressing DSR2 and SPR TTP when induced at different ratio between IPTG to L-Ara (indicated on top). NAD⁺ measurements were taken every 20 min, and each curve represents the mean \pm SD of

$n = 3$ independent biological replicates. **d** NADase activity of DSR2-TTP complexes harboring indicated mutations at five key regions: the DSR2 CTD-SIR2 interface (red background), the SIR2-SIR2 interface (yellow background), the DSR2-TTP interface on TTP (blue background), the DSR2-TTP interface on DSR2 (gray background) and the DSR2-DSR2 interface (green background). Data is presented as mean \pm SD from $n = 3$ independent biological replicates. **e** Cryo-EM structure of the DSR2-TTP complex illustrating five key regions for mutagenesis; residues involved in mutagenesis are shown with spheres and colored as in **(d)**. While the DSR2-TTP complex is colored gray, the top right DSR2 is highlighted cyan and the top right TTP is highlighted dark blue. **f** A working model for activation mechanism of DSR2 system.

Methods

Plasmid construction and protein purification

The genes encoding *Bacillus subtilis* DSR2 (NCBI Reference Sequence: WP_029317421.1) and the *Bacillus* phage SPR tail tube protein (TTP; GenBank: UNY48585.1) were synthesized by GenScript (Table S3). To

assemble the DSR2-SPR TTP complex, the genes of DSR2 and SPR TTP were inserted into the pETDuet-1 vector between NdeI/XhoI and NcoI/HindIII restriction sites, respectively. A 6 \times His tag was added to the C-terminus of SPR TTP via PCR primers (Table S4); DSR2 did not have any affinity tags. The two components were then co-expressed in BL21 (DE3)

competent cells. The most stable DSR2-SPR TTP complex was obtained by introducing an H171A mutation in DSR2 and was used for structural studies. For DSR2 alone expression, DSR2 gene was cloned into a pET28a-SUMO plasmid pre-cut with BamHI and XhoI. The plasmid was transformed into BL21(DE3) grown in Luria-Broth (LB) medium to an $OD_{600} \sim 0.7$; the medium was subsequently induced by adding 0.25 mM isopropyl β -D-1-thiogalactopyranoside (IPTG) and the culturing continued at 18 °C overnight.

To purify the recombinant proteins, bacteria cultures were centrifuged at $4000 \times g$ for 10 min and the pellet suspended in lysis buffer (40 mM Tris-HCl, pH = 8.0, 10 mM imidazole, 150 mM NaCl and 1 mM phenylmethylsulfonyl fluoride). Bacteria cells were then lysed by ultrasonication and clarified by centrifugation at $25,000 \times g$ for 50 min at 4 °C. The supernatant was applied to Ni-NTA resins (QIAGEN) under gravity. To remove nonspecifically bounded material, $3 \times$ column volumes of the wash buffer (40 mM Tris-HCl, pH = 8.0, 20 mM imidazole and 150 mM NaCl) were loaded. The target protein was finally eluted with the elution buffer (25 mM Tris-HCl, pH = 8.0, 300 mM imidazole and 50 mM NaCl). For DSR2 protein, its N-terminal His-SUMO tag was cleaved from the DSR2 protein by the Ulp1 protease, and the untagged DSR2 was collected by passing through a Ni-NTA column.

The DSR2-SPR TTP complex or DSR2 protein was further purified by loading onto a HiTrap Q HP column (GE Healthcare) pre-equilibrated with the buffer A (25 mM Tris-HCl, pH = 8.0 and 25 mM NaCl). The protein was then eluted with a linear salt gradient from buffer A to buffer B (25 mM Tris-HCl, pH = 8.0 and 1 M NaCl). Fractions containing the target protein were pooled and concentrated before loading onto Superdex 200 10/300 increase column (Cytiva) pre-equilibrated with a buffer containing 20 mM Tris pH = 8.0 and 100 mM NaCl.

For expression in *E. coli* MG1655 or BL21-AI, DSR2, DSR2-H171A and DSR2-N133A-H171A were cloned into pACYCDuet-1 vector between BamHI/HindIII restriction sites, respectively. The SPR tail tube protein (TTP) was cloned into pBAD-Myc-His vector between NcoI/HindIII restriction sites and added a TAA stop codon at the end of TTP to prevent the expression of Myc-His.

Cryo-EM sample preparation

Finally purified DSR2, DSR2-SPR TTP and DSR2-SPR TTP complexes incubated with 5 mM NAD^+ were concentrated to 0.3 ~ 0.5 mg/mL. For all samples, 3 μ L of protein was applied immediately to glow discharged Quantifoil R1.2/1.3 holey carbon Cu 300-mesh grids. After a 7 s wait, 4 s blotting by a FEI vitrobot was performed under 100% humidity at 4 °C. The grids were then plunge-frozen in liquid ethane, which had been pre-cooled by liquid nitrogen.

Cryo-EM data collection and analysis

All datasets were collected at the Center for Biological Imaging, Core Facilities for Protein Science, Institute of Biophysics, Chinese Academy of Sciences following the same procedure. Briefly, the movies were recorded on a FEI Titan Krios, equipped with a K3 detector at an acceleration voltage of 300 kV, at a nominal magnification of 29,000 with a pixel size of 0.83 Å. The defocus range was set in the range of -1.5 to -2.5 μ m. The movies were collected by SerialEM^{41,42} or EPU with a total dose of 66 $e^-/\text{Å}^2$.

For the DSR2 alone dataset, a total of 6314 movies were collected and subsequently subjected to motion correction⁴³ and CTF estimation⁴⁴ in cryoSPARC-3.3.2⁴⁵. Firstly, 20 micrographs without ice contamination and with low astigmatism were handpicked for particle selection. About 300 good particles were picked for training with Topaz⁴⁶. After Topaz extraction, 2D classification was carried out for the 2,054,396 Topaz extracted particles. Promising 2D classes were then selected for a round of ab initio reconstruction. The 3D model featuring DSR2 characteristics was then selected for further heterogeneous refinement using the raw particles extracted by Topaz. After two rounds of heterogeneous refinement, the tetramer and/ or tetramer fragment were further selected for one round of non-uniform

refinement, resulting in final maps with the resolution of 4.53 Å and 3.74 Å, respectively.

For the DSR2-SPR TTP complex with NAD^+ dataset, a total of 6012 movies were collected. Following motion correction and CTF estimation^{43,44}, Blob picker and Particle inspection were carried out in cryoSPARC-3.3.2⁴⁵. Approximately 2.5 million particles were extracted, and 2D classification was employed to identify high-quality particles. To solve the cryo-EM structure of SPR TTP bound DSR2 CTD pair with NAD^+ , particles of interest were selected based on the outcomes of 2D classification. A round of non-uniform refinement was conducted using the best ab initio model as input. To solve the cryo-EM structure of SPR tail tube complex, the associated particles were first selected as indicated by the 2D classification. The centers of particles were then adjusted manually on the first 20 micrographs, followed by Topaz training and extraction⁴⁶. After removing the junk particles through one round of 2D classification, one round of ab initio reconstruction was used to obtain an initial model. Subsequently, the best model, together with the particles extracted by Topaz⁴⁶, was used for one round of heterogeneous refinement. The class featuring high-resolution characteristics was chosen for a final round of non-uniform refinement. Regarding the tetramer and/ or tetramer fragment with NAD^+ , the center of the particles was adjusted manually after the ab initio reconstruction. The center re-adjusted particles were then used for Topaz training and extraction⁴⁶. Another round of ab initio reconstruction was then performed to obtain a well-centered tetramer map. The yielded tetramer map and the particles picked by Topaz then functioned as the input for one round of heterogeneous refinement. As for the tetramer fragment, one round of non-uniform refinement was performed after the heterogeneous refinement. Meanwhile, the particles belonging to the tetramer fragment class were re-centered, followed by a final run of non-uniform refinement. The resolutions for SPR TTP bound DSR2 CTD pair with NAD^+ , SPR tail tube complex, SPR TTP bound DSR2 tetramer fragment with NAD^+ and SPR TTP bound DSR2 tetramer with NAD^+ were 3.29 Å, 3.43 Å, 4.27 Å and 4.40 Å, respectively.

For the DSR2-SPR TTP complex without NAD dataset, 4693 movies were collected. After motion correction and CTF estimation^{43,44} in cryoSPARC-3.3.2⁴⁵, about 350 particles were picked manually from 20 good micrographs. Next, Topaz training was performed followed by Topaz extraction⁴⁷; 1,008,211 particles were picked and extracted. One round of 2D classification was then performed to get rid of these junk particles. Based on the features of the 2D classes, the particles belonging to SPR TTP bound DSR2 CTD pair and SPR TTP bound DSR2 tetramer classes were selected respectively. We first solved the structure of SPR TTP bound DSR2 CTD pair initialized with one round of ab initio reconstruction. The 3D model with the highest resolution was selected for further non-uniform refinement. Similarly, an ab initio reconstruction was performed for particles belonging to SPR TTP bound DSR2 tetramer, and the best class showing the feature of SPR TTP bound DSR2 tetramer fragment was selected followed by two rounds of heterogeneous refinement. The particles belonging to SPR TTP bound DSR2 tetramer or tetramer fragment were combined for a further non-uniform refinement. The final resolutions for SPR TTP bound DSR2 CTD pair, SPR TTP bound DSR2 tetramer or tetramer fragment were 3.78 Å, 4.66 Å and 4.03 Å.

All of the maps were finally sharpened by DeepEMhancer⁴⁸. No symmetry was applied for the cryo-EM data analysis.

Model building

A homology model for DSR2 was generated by AlphaFold2 (AF2)⁴⁹. The model generated by AlphaFold2 did not align perfectly with the maps due to domain movements; therefore, the DSR2 model was divided into three distinct domains, each of which was fitted into the map separately. For the DSR2 tetramer and/ or tetramer fragment, the initial model was generated by rigid body fitting of four or two DSR2 molecules into the density map separately using UCSF Chimera⁵⁰. The chain IDs were then re-assigned in Coot⁵¹. The models were then manually adjusted in Coot⁵¹ followed by real-space refinement in PHENIX⁵². The final map to model validations was

performed using the comprehensive validation tool (cryo-EM) in PHENIX with a cc value for tetramer fragment and/or tetramer of 0.70 and 0.73, respectively⁵².

To build the models for DSR2-SPR TTP with or without NAD⁺, the homology model for SPR TTP was generated by Alpha Fold2⁴⁹. Due to the lack of resolved density in the map for residues beyond 78 in the TTP model, we opted to utilize the portion of the predicted TTP model ranging from residues 1 to 78. To build DSR2-SPR TTP tetramer and/or tetramer fragment, a process similar to that used for building the DSR2 tetramer and/or tetramer fragment was employed, UCSF Chimera was first used to obtain the initial models⁵⁰. Coot was then used to adjust the models manually based on the features of the maps⁵¹. PHENIX real-space refinement was finally used to refine the models⁵². The final map to model cc values for DSR2-SPR TTP tetramer fragment and tetramer were 0.69 and 0.65 based on the comprehensive validation tool (cryo-EM) in PHENIX⁵². To build a model of the SPR TTP bound DSR2 CTD pair, the DSR2 structure encompassing residues 298–1005 and the TTP structure spanning residues 1–78 were chosen from the DSR2-SPR TTP tetramer fragment followed by a rigid body fitting in UCSF Chimera⁵⁰. After one round of manual adjustment in Coot⁵¹, PHENIX real-space refinement was used to refine the model⁵². Following a thorough validation process using cryo-EM in PHENIX. The final cc values between the maps and models of the SPR TTP bound DSR2 CTD pair and SPR TTP bound DSR2 CTD pair with NAD⁺ were 0.44 and 0.68, respectively.

To build the models for SPR tail tube complex, Initially, the predicted SPR TTP structure was first divided into two segments: TTP-head (1–78) and TTP-tail (79–241). UCSF Chimera was then used to isolate the monomeric form of SPR-TTP map. Subsequently, the TTP-head and TTP-tail segments were subjected to rigid body fitting to the isolated TTP monomer map. Next, Coot was used to combine the two parts to produce a new TTP model⁵¹. The newly generated TTP model was then fitted to the SPR tail tube complex map in UCSF Chimera⁵⁰. A total of 18 SPR TTP monomers were integrated successfully into the SPR tail tube complex density map. Given the strong correspondence between the TTP models and the density, a round of PHENIX real-space refinement was performed to refine the model⁵². The map to model cc value was 0.75, calculated by comprehensive validation tool (cryo-EM) in PHENIX⁵².

Cell viability assay

Cell viability assay was conducted as previously described⁵³. Briefly, plasmids pBAD-TTP and pACYCDuet-DSR2 (wild-type or mutant variants) were co-transformed into *E. coli* BL21-AI or MG1655, respectively. The strains were overnight cultured in 3 mL MMB medium (LB + 0.1 mM MnCl₂ + 5 mM MgCl₂) supplemented with 1% glucose, 25 µg/mL chloramphenicol and 100 µg/mL carbenicillin, and then transferred 1:100 into 3 mL MMB medium, incubating at 37 °C until OD₆₀₀ = 0.3. Subsequently, a tenfold serial dilution was performed, and 5 µL of the bacterial culture from each concentration was spotted onto LB plates containing inducers (+1 mM IPTG, 0.2% L-Ara) or without inducers. After incubating overnight at 37 °C, photos were taken.

In vivo growth curve assays

The MG1655 cells containing pACYCDuet-DSR2 and pBAD-TTP were overnight cultured in MMB medium supplemented with 1% glucose, 25 µg/mL chloramphenicol and 100 µg/mL carbenicillin, and were diluted 1:100 into 3 mL of MMB medium the next day. Then incubated at 37 °C, 200 rpm to OD₆₀₀ = 0.3, and then 1 mM IPTG, 0.2% L-Ara, or no inducer was added. 200 µL of the culture was transferred into a 96-well cell culture plate (Corning, 3599). The plate was placed in a SpectraMax iD5 (Molecular Devices) and cultured at 37 °C with shaking, measuring the OD₆₀₀ every 10 min.

Intracellular NAD⁺ levels measurement

The intracellular NAD⁺ levels were measured as described previously^{54–57}. In brief, *E. coli* MG1655 harboring TTP and DSR2 or DSR2 mutants, or control

plasmid, were overnight cultured in MMB medium supplemented with 1% glucose, 25 µg/mL chloramphenicol and 100 µg/mL carbenicillin. Cells were back-diluted 100-fold into 5 mL MMB medium and grown at 37 °C 220 rpm to OD₆₀₀ ~ 0.3. Then 1 mM IPTG and 0.2% L-Ara were added to induce DSR2 and TTP, respectively. Samples of 800 µL culture were then collected at times 0, 20, 40, 60 min after inducing and centrifuged at 4 °C, 12,000 rpm for 1 min. The supernatant was discarded and the cell pellets were frozen in liquid nitrogen for preservation. For NAD⁺ measure, cell pellets were resuspended in 200 µL PBS and were lysed with a solution containing 0.2 M NaOH and 1% (w/v) cetyltrimethylammonium bromide (CTAB, Sigma). Subsequently, the lysed samples were exposed to 0.4 M HCl at 60 °C for 15 min. Finally, the samples were neutralized with 0.5 M Tris base and mixed with an equal amount of NAD⁺/NADH-Glo™ Detection Reagent (Promega) as the protocol described. After a 30-min incubation, luminescence was measured with a microplate reader (SpectraMax iD5, Molecular Devices). The relative NAD⁺ concentrations were calculated from the calibration curve using a set of standard NAD⁺ samples with known concentrations.

In vitro NADase activity assay

The in vitro NADase activity was measured using an NAD fluorescent analog εNAD⁺ as the substrate. Upon reaction, the product εADPR serves as a fluorophore for fluorescence detection and quantification (excitation wavelength at 310 nm and emission wavelength at 410 nm). Each reaction (60 µL) was prepared with reaction buffer (10 mM MES pH 7.5, 75 mM KCl, 2 mM MgCl₂) and 100 µM εNAD⁺ (Sigma Aldrich, N2630) in the beginning. Then 1 µM DSR2 (WT or mutants) and 5 µM TTP (WT or mutants) were added to activate the reaction. The reaction mixtures were loaded into Greiner 96-well half-area plates, and fluorescence was measured continuously for 120 min with 2 min intervals on a microplate reader (SpectraMax iD5, Molecular Devices). All reactions were conducted at 37 °C. A calibration curve was plotted using the data measured for 120 min of reaction with 6.25, 12.5, 25, 50, 100 and 200 µM of εNAD⁺ as the initial concentration. All experiments were repeated three times with mean values and standard deviations.

Statistics and data reproducibility

Statistical analyses and data summarization were performed using Graph-Pad Prism 10.2. All data are presented as the mean ± standard deviation (SD) from three independent biological replicates. Each biological replicate represents an independent experiment conducted under the same conditions to ensure reproducibility.

Reporting summary

Further information on research design is available in the Nature Portfolio Reporting Summary linked to this article.

Data availability

The atomic models of free-state DSR2 tetramer fragment, free-state DSR2 tetramer, SPR TTP bound DSR2 CTD pair, SPR TTP bound DSR2 tetramer fragment, SPR TTP bound DSR2 tetramer, SPR TTP bound DSR2 CTD pair with NAD⁺, SPR TTP bound DSR2 tetramer fragment with NAD⁺, SPR TTP bound DSR2 tetramer with NAD⁺ and SPR tail tube complex have been deposited into the Protein Data Bank with accession code 8YG1, 8YGA, 8YGG, 8YGC, 8YGF, 8YGO, 8YGN, 8YGP, and 8YGM, respectively. The corresponding 3D cryo-EM density maps have been deposited into the Electron Microscopy Data Bank under the accession codes EMD-39233, EMD-39240, EMD-39254, EMD-39243, EMD-39246, EMD-39258, EMD-39257 and EMD-39259, respectively. The source data behind the Fig. 5 are shown in Supplementary Data. All other datasets generated and/or analyzed during this study are available from the corresponding author upon reasonable request.

Received: 1 August 2024; Accepted: 14 February 2025;

Published online: 24 February 2025

References

- Georjon, H. & Bernheim, A. The highly diverse antiphage defence systems of bacteria. *Nat. Rev. Microbiol.* **21**, 686–700 (2023).
- Doron, S. et al. Systematic discovery of antiphage defense systems in the microbial pangenome. *Science* **359**, eaar4120 (2018).
- Gao, L. et al. Diverse enzymatic activities mediate antiviral immunity in prokaryotes. *Science* **369**, 1077–1084 (2020).
- Gao, Y. et al. Molecular basis of RADAR anti-phage supramolecular assemblies. *Cell* **186**, 999–1012.e1020 (2023).
- Wang, Y. et al. Cryo-EM structures of *Escherichia coli* Ec86 retron complexes reveal architecture and defence mechanism. *Nat. Microbiol.* **7**, 1480–1489 (2022).
- Duncan-Lowey, B. et al. Cryo-EM structure of the RADAR supramolecular anti-phage defense complex. *Cell* **186**, 987–998.e915 (2023).
- Hsueh, B. Y. et al. Phage defence by deaminase-mediated depletion of deoxynucleotides in bacteria. *Nat. Microbiol.* **7**, 1210–1220 (2022).
- Ka, D., Oh, H., Park, E., Kim, J. H. & Bae, E. Structural and functional evidence of bacterial antiphage protection by Thoeris defense system via NAD⁺ degradation. *Nat. Commun.* **11**, 2816 (2020).
- Rousset, F. et al. A conserved family of immune effectors cleaves cellular ATP upon viral infection. *Cell* **186**, 3619–3631.e3613 (2023).
- Shen, Z., Lin, Q., Yang, X. Y., Fosuah, E. & Fu, T. M. Assembly-mediated activation of the SIR2–HerA supramolecular complex for anti-phage defense. *Mol. Cell* **83**, 4586–4599.e4585 (2023).
- Tal, N. et al. Bacteria deplete deoxynucleotides to defend against bacteriophage infection. *Nat. Microbiol.* **7**, 1200–1209 (2022).
- Tang, D. et al. Multiple enzymatic activities of a Sir2–HerA system cooperate for anti-phage defense. *Mol. Cell* **83**, 4600–4613.e4606 (2023).
- Cohen, D. et al. Cyclic GMP–AMP signalling protects bacteria against viral infection. *Nature* **574**, 691–695 (2019).
- Whiteley, A. T. et al. Bacterial cGAS-like enzymes synthesize diverse nucleotide signals. *Nature* **567**, 194–199 (2019).
- Millman, A., Melamed, S., Amitai, G. & Sorek, R. Diversity and classification of cyclic-oligonucleotide-based anti-phage signalling systems. *Nat. Microbiol.* **5**, 1608–1615 (2020).
- Duncan-Lowey, B., McNamara-Bordewick, N. K., Tal, N., Sorek, R. & Kranzusch, P. J. Effector-mediated membrane disruption controls cell death in CBASS antiphage defense. *Mol. Cell* **81**, 5039–5051.e5035 (2021).
- Johnson, A. G. et al. Bacterial gasdermins reveal an ancient mechanism of cell death. *Science* **375**, 221–225 (2022).
- Zeng, Z. et al. A short prokaryotic Argonaute activates membrane effector to confer antiviral defense. *Cell Host Microbe* **30**, 930–943.e936 (2022).
- Bernheim, A. et al. Prokaryotic viperins produce diverse antiviral molecules. *Nature* **589**, 120–124 (2021).
- Chi, H. et al. Antiviral type III CRISPR signalling via conjugation of ATP and SAM. *Nature* **622**, 826–833 (2023).
- Millman, A. et al. Bacterial retrons function in anti-phage defense. *Cell* **183**, 1551–1561.e1512 (2020).
- Bobonis, J. et al. Bacterial retrons encode phage-defending tripartite toxin-antitoxin systems. *Nature* **609**, 144–150 (2022).
- Zaremba, M. et al. Short prokaryotic Argonautes provide defence against incoming mobile genetic elements through NAD⁺ depletion. *Nat. Microbiol.* **7**, 1857–1869 (2022).
- Ofir, G. et al. Antiviral activity of bacterial TIR domains via immune signalling molecules. *Nature* **600**, 116–120 (2021).
- Garb, J. et al. Multiple phage resistance systems inhibit infection via SIR2-dependent NAD⁺ depletion. *Nat. Microbiol.* **7**, 1849–1856 (2022).
- North, B. J. & Verdin, E. Sirtuins: Sir2-related NAD-dependent protein deacetylases. *Genome Biol.* **5**, 224 (2004).
- Gallejo-Jara, J. et al. Bacterial sirtuins overview: an open niche to explore. *Front. Microbiol.* **12**, 744416 (2021).
- Zhen, X. et al. Structural basis of antiphage immunity generated by a prokaryotic Argonaute-associated SPARSA system. *Nat. Commun.* **15**, 450 (2024).
- Manik, M. K. et al. Cyclic ADP ribose isomers: production, chemical structures, and immune signaling. *Science* **377**, eadc8969 (2022).
- Tamulaitiene, G. et al. Activation of Thoeris antiviral system via SIR2 effector filament assembly. *Nature* **627**, 431–436 (2024).
- Béchon, N. et al. Diversification of molecular pattern recognition in bacterial NLR-like proteins. *Nat. Commun.* **15**, 9860 (2024).
- Gao, L. A. et al. Prokaryotic innate immunity through pattern recognition of conserved viral proteins. *Science* **377**, eabm4096 (2022).
- Holm, L. Dali server: structural unification of protein families. *Nucleic Acids Res.* **50**, W210–W215 (2022).
- Kohm, K. & Hertel, R. The life cycle of SPβ and related phages. *Arch. Virol.* **166**, 2119–2130 (2021).
- Kajava, A. V. Tandem repeats in proteins: from sequence to structure. *J. Struct. Biol.* **179**, 279–288 (2012).
- Kibby, E. M. et al. Bacterial NLR-related proteins protect against phage. *Cell* **186**, 2410–2424.e2418 (2023).
- Marchand, J. R., Pirard, B., Ertl, P. & Sirockin, F. CAVIAR: a method for automatic cavity detection, description and decomposition into subcavities. *J. Comput. Aided Mol. Des.* **35**, 737–750 (2021).
- Zhang, J. T. et al. Structural basis for phage-mediated activation and repression of bacterial DSR2 anti-phage defense system. *Nat. Commun.* **15**, 2797 (2024).
- Huang, J. et al. Molecular basis of bacterial DSR2 anti-phage defense and viral immune evasion. *Nat. Commun.* **15**, 3954 (2024).
- Yin, H. et al. Insights into the modulation of bacterial NADase activity by phage proteins. *Nat. Commun.* **15**, 2692 (2024).
- Wu, C., Huang, X., Cheng, J., Zhu, D. & Zhang, X. High-quality, high-throughput cryo-electron microscopy data collection via beam tilt and astigmatism-free beam-image shift. *J. Struct. Biol.* **208**, 107396 (2019).
- Mastronarde, D. N. Automated electron microscope tomography using robust prediction of specimen movements. *J. Struct. Biol.* **152**, 36–51 (2005).
- Zheng, S. Q. et al. MotionCor2: anisotropic correction of beam-induced motion for improved cryo-electron microscopy. *Nat. Methods* **14**, 331–332 (2017).
- Rohou, A. & Grigorieff, N. CTFFIND4: fast and accurate defocus estimation from electron micrographs. *J. Struct. Biol.* **192**, 216–221 (2015).
- Punjani, A., Rubinstein, J. L., Fleet, D. J. & Brubaker, M. A. cryoSPARC: algorithms for rapid unsupervised cryo-EM structure determination. *Nat. Methods* **14**, 290–296 (2017).
- Bepler, T. et al. Positive-unlabeled convolutional neural networks for particle picking in cryo-electron micrographs. *Nat. Methods* **16**, 1153–1160 (2019).
- Bepler, T. et al. Positive-unlabeled convolutional neural networks for particle picking in cryo-electron micrographs. *Res. Comput. Mol. Biol.* **10812**, 245–247 (2018).
- Sanchez-Garcia, R. et al. DeepEMhancer: a deep learning solution for cryo-EM volume post-processing. *Commun. Biol.* **4**, 874 (2021).
- Jumper, J. et al. Highly accurate protein structure prediction with AlphaFold. *Nature* **596**, 583–589 (2021).
- Pettersen, E. F. et al. UCSF Chimera—a visualization system for exploratory research and analysis. *J. Comput. Chem.* **25**, 1605–1612 (2004).
- Emsley, P., Lohkamp, B., Scott, W. G. & Cowtan, K. Features and development of Coot. *Acta Crystallogr. D Biol. Crystallogr.* **66**, 486–501 (2010).

52. Adams, P. D. et al. PHENIX: a comprehensive Python-based system for macromolecular structure solution. *Acta Crystallogr. D Biol. Crystallogr.* **66**, 213–221 (2010).
53. Sun, D. et al. Nucleic acid-induced NADase activation of a short Sir2-associated prokaryotic Argonaute system. *Cell Rep.* **43**, 114391 (2024).
54. Tang, J. Y., Bullen, N. P., Ahmad, S. & Whitney, J. C. Diverse NADase effector families mediate interbacterial antagonism via the type VI secretion system. *J. Biol. Chem.* **293**, 1504–1514 (2018).
55. Skjerming, R. B., Senissar, M., Winther, K. S., Gerdes, K. & Brodersen, D. E. The RES domain toxins of RES-Xre toxin-antitoxin modules induce cell stasis by degrading NAD⁺. *Mol. Microbiol.* **111**, 221–236 (2019).
56. Freire, D. M. et al. An NAD⁺ phosphorylase toxin triggers *Mycobacterium tuberculosis* cell death. *Mol. Cell* **73**, 1282–1291.e1288 (2019).
57. Osterman, I. et al. Phages reconstitute NAD⁺ to counter bacterial immunity. *Nature* **634**, 1160–1167 (2024).

Acknowledgements

We thank X. Huang, B. Zhu, X. Li, L. Chen, T. Niu and other staff members at the Center for Biological Imaging (CBI), Core Facilities for Protein Science at the Institute of Biophysics, Chinese Academy of Science (IBP, CAS) for the support in cryo-EM data collection. We thank Z.Q. Guo and H.S. Li from Shuimu Biosciences for the cryo-EM data collection. We thank the staff from the Core Facility of the National Institute of Pathogen Biology, Chinese Academy of Medical Sciences. This work was supported by National Key Research and Development Program of China (2023YFC2307800); Chinese Academy of Medical Sciences (CAMS) Innovation Fund for Medical Sciences (2021-I2M-1-037); the Non-profit Central Research Institute Fund of Chinese Academy of Medical Sciences (2023-PT310-04); National Natural Science Foundation of China (82341095, 82261160398, 82272308, 82402596, 32471015); the Fundamental Research Funds for the Central Universities (3332021092); Chinese Academy of Sciences (No. E4V4061RA1, E2VK311RA1).

Author contributions

S.C. and X.G. designed the study. S.C., H.Z. and X.G. solved the EM structures and performed the model building. S.C., X.G. and H.Z. wrote the paper. X.G., K.S., K.Z., L.W., X.Y., L.H., W.Z., J.W. and B.Q. performed experiments and analyzed the data. All authors reviewed the results and approved the final version of the manuscript.

Competing interests

The authors declare no competing interests.

Additional information

Supplementary information The online version contains supplementary material available at <https://doi.org/10.1038/s42003-025-07743-3>.

Correspondence and requests for materials should be addressed to Xiaopan Gao, Hongtao Zhu or Sheng Cui.

Peer review information *Communications Biology* thanks Dipshikha Chakravorty and the other anonymous reviewer(s) for their contribution to the peer review of this work. Primary handling editors: Tobias Goris. A peer review file is available.

Reprints and permissions information is available at <http://www.nature.com/reprints>

Publisher's note Springer Nature remains neutral with regard to jurisdictional claims in published maps and institutional affiliations.

Open Access This article is licensed under a Creative Commons Attribution-NonCommercial-NoDerivatives 4.0 International License, which permits any non-commercial use, sharing, distribution and reproduction in any medium or format, as long as you give appropriate credit to the original author(s) and the source, provide a link to the Creative Commons licence, and indicate if you modified the licensed material. You do not have permission under this licence to share adapted material derived from this article or parts of it. The images or other third party material in this article are included in the article's Creative Commons licence, unless indicated otherwise in a credit line to the material. If material is not included in the article's Creative Commons licence and your intended use is not permitted by statutory regulation or exceeds the permitted use, you will need to obtain permission directly from the copyright holder. To view a copy of this licence, visit <http://creativecommons.org/licenses/by-nc-nd/4.0/>.

© The Author(s) 2025